The University Of Sheffield.

This is a repository copy of *On the nitrogen-induced lattice expansion of a non-stainless austenitic steel, Invar 36®, under triode plasma nitriding*.

White Rose Research Online URL for this paper:
http://eprints.whiterose.ac.uk/154515/

Version: Accepted Version

Article:

1 **On the nitrogen-induced lattice expansion of a non-stainless austenitic steel,**

2 **Invar 36®, under Triode Plasma Nitriding**

3

4 Authors:

5 Xiao Tao[a,c], Allan Matthews[b], Adrian Leyland[a]

6

7 [a] Department of Materials Science and Engineering, The University of Sheffield,

8 Sheffield, S1 3JD, UK

9 [b] School of Materials, The University of Manchester, Manchester, M13 9PL, UK

10 [c] School of Metallurgy and Materials, University of Birmingham, Birmingham B15

11 2TT, UK

12

13 Xiao Tao, email: x.tao@bham.ac.uk

14 Allan Matthews, email: allan.matthews@manchester.ac.uk

15 Adrian Leyland, email: a.leyland@sheffield.ac.uk

16

17

18 *Corresponding author: Dr. Adrian Leyland

19 Email: a.leyland@sheffield.ac.uk

20 Telephone: +44 (0) 114 222 5486

21 Fax: +44 (0) 114 222 5943

22 Full postal address: Department of Materials Science and Engineering, Sir Robert

23 Hadfield Building, Mappin Street, Sheffield, S1 3JD, United Kingdom

24 **Abstract**

25 Chromium, as a strong nitride forming element, is widely regarded to be an 'essential'

26 ingredient for the formation of a nitrogen-expanded lattice in thermochemical

27 nitrogen diffusion treatments of austenitic (stainless) steels. In this paper, a

28 proprietary 'chrome-free' austenitic iron-nickel alloy, Invar® 36 (Fe-36Ni, in wt.%),

29 is characterised after Triode-Plasma Nitriding (TPN) treatments at 400-450°C and

30 compared to a 'stainless' austenitic counterpart RA 330® (Fe-19Cr-35Ni, in wt.%)

31 treated under equivalent nitriding conditions. Cr does indeed appear to play a pivotal

32 role in colossal nitrogen supersaturation (and hence, anisotropic lattice expansion and

33 superior surface hardening) of austenitic steel under low-temperature (≤ 450°C)

34 nitrogen diffusion. Nevertheless, this work reveals that nitrogen-induced lattice

35 expansion occurs below the nitride-containing surface layer in Invar 36 alloy after

36 TPN treatment, implying that Cr is not a necessity for the nitrogen-interstitial induced

37 lattice expansion phenomenon to occur, also suggesting another type of γ_N.

38

39 Keywords: austenitic steel; expanded austenite; plasma nitriding

1 Introduction

After early scientific studies published by Bell et al. [1] and Ichii et al. [2] in the 1980s, low temperature plasma diffusion treatments have been widely investigated as a potential solution to the poor tribological performance of Austenitic Stainless Steels (ASSs) [3-7]. Nitrogen-expanded austenite [3] (γ_N; also called "S-phase" [2]) can be synthesised on ASSs (such as AISI 304, 310 and 316 type alloys, based mainly on the Fe-Cr-Ni ternary alloy system) under low temperature ($\leq 450°C$) nitriding without the formation of chromium nitride, where the original face-centred cubic (FCC) structure is expanded anisotropically under extremely high interstitial nitrogen uptake [8-10]. Recent studies of expanded austenite (γ_N) have focused on the crystallographic structure of N-supersaturated ASS surfaces [11-18]; however, there are still uncertainties about the roles of the primary substitutional alloying elements (e.g. Cr, Ni and/or Mn) in the formation of γ_N during low temperature thermochemical diffusion treatment. This topic can be traced back to the 1990s, when authors such as Menthe et al. [19] and Yasumaru [20] reported that γ_N does not form in steels containing either Cr or Ni/Mn alone (i.e. Fe-13Cr-0.2C, Fe-17Cr-0.1C, Fe-30Ni, Fe-32Ni, Fe-42Ni and Fe-26Mn-0.2C, in wt.%) under low-temperature nitriding. It was argued that both Cr and Ni/Mn are necessary for the formation of γ_N on austenitic steels. More recently, however, Buhagiar et al. [13] and Tao et al. [18] reported the formation of γ_N on Ni-free high-Mn ASSs, proving unequivocally that neither Ni nor Mn are in themselves crucial for the formation of γ_N (although each may affect differently the nitrogen supersaturation levels obtained, the lattice plasticity mechanisms and the γ_N lattice (in)stability observed with increasing treatment temperature/time [18]).

On the other hand, Cr − as a strong nitride forming element − is widely believed to be an 'essential' component of the substrate alloy composition for γ_N formation (with appropriate

1

65   mechanical/tribological/corrosion resistant properties) [21, 22]. Expanded austenite has been

66   synthesised using various low-temperature nitrogen surface modification techniques on

67   Fe/Ni/Co-based alloys with substrate Cr content ranging from ~13 at.% (for proprietary

68   precipitation hardening stainless steels, such as Nanoflex® and Corrax® [23]) to ~31 at.%

69   (for a special Co-Cr alloy [24]). A significant amount of Cr (as a 'nitrogen trapper') in the

70   substrate (i.e. $\geq$ 12 at.%, also typical for stainless steels to promote the stable surface

71   chromium oxide layer formation) appears to be important in the formation of 'useful' γ_N

72   under low-temperature nitrogen surface modification. The role of Cr has been investigated

73   and discussed in several studies of γ_N-304 and/or γ_N-316, which have pointed to 'trapping and

74   detrapping' diffusion of N [25, 26] and to the bonding (and short-range ordering) of N to Cr

75   [19, 27, 28]. It was postulated that Cr could provide trap sites for N, contributing to the

76   extremely high interstitial absorption and anomalous (anisotropic) lattice expansion of ASSs,

77   seen under low-temperature nitriding [10, 22, 28]. Additionally, pure γ-Ni clearly shows no

78   lattice expansion under nitrogen ion implantation [29, 30], but γ_N was reported (with evident

79   XRD peak shifts to lower 2θ angles) after nitrogen surface modification treatments on Ni-

80   alloys that contain strong-nitride formers, such as Ni-Cr binary alloys (containing ~20 at.%

81   Cr [29, 30] and ~26 at.% Cr [31]), Ni-Ti binary alloys (containing ~1.6 at.% Ti [32], ~3.3 at.%

82   Ti [32] and ~5.8 at.% Ti [31]), and a range of commercial Cr-containing Ni-superalloys [29].

83   While a (meta)stable austenitic substrate microstructure alone appears an insufficient

84   requirement, strong-nitride-formers appear to be a necessity for the formation of γ_N on

85   Fe/Ni/Co-based substrates.

86

87   Nevertheless, Williamson et al. [29] reported 'highly-expanded' and 'less-expanded' FCC

88   phases (designated as γ_{N1} and γ_{N2}, respectively, in their paper) on a Cr-free high-Ni Invar

89   alloy (Fe-35Ni, in wt.%) after N-implantation at 400°C, which appears to be contradictory

90 (and hence intriguing) to the widely-reported 'essential' role played by Cr in austenite lattice

91 expansion under low-temperature nitrogen diffusion treatment. However, apart from surface

92 XRD profiles, no further details were given in [29] on the structure of expanded austenitic

93 phases synthesised on Fe-35Ni. Alloy RA 330® (Fe-19Cr-35Ni, in wt.%), as a high-Ni

94 stainless counterpart of Fe-35Ni, was previously characterised by the authors of the present

95 work after triode-plasma nitriding (TPN) [18]. To investigate the γ_{N1} and γ_{N2} phases reported

96 in [29] and to elucidate the role of Cr, a TPN-treated non-stainless high-Ni austenitic steel,

97 Invar 36® (Fe-36Ni, in wt.%), is investigated in this study and compared (under equivalent

98 treatment conditions) to the TPN-treated alloy RA 330.

99

100 **2   Experimental**

101 The chemical compositions of Invar 36® (City Special Metals Ltd. Sheffield, UK) and RA

102 330® (Neonickel Ltd. Blackburn, UK) are presented in **Table 1**. Disks of 20 mm diameter

103 (and 3 mm thick) were sliced from a solution-annealed bar of alloy Invar 36 using an

104 abrasive cutting wheel (Struers Secotom-50). Rectangular RA 330 alloy coupons of

105 dimensions ~25×25×4 mm were cut from 4 mm thick solution-annealed plates. Invar 36

106 samples were plasma nitrided in a modified commercial PVD coating unit, Tecvac IP70L,

107 using a triode-plasma nitriding (TPN) configuration [3, 33, 34] under a treatment pressure of

108 0.4 Pa (with N_2:Ar gas volume ratio of 7:3) and substrate bias of -200 V, at 400°C, 425°C

109 and 450°C for 4hrs and 20hrs, respectively. The precise sample preparation and nitriding

110 treatment procedures are described in detail in Ref. [18].

111

112 A Nikon Eclipse LV150 optical microscope (OM) was used for optical imaging and a Philips

113 XL30S FEG electron microscope (with Oxford Instruments INCA EDX system) for Energy

114 Dispersive X-ray (EDX) spectroscopy. Beam acceleration voltage and spot size were 15kV

and 5, respectively. Beam intensity was calibrated with a cobalt standard before each

measurement. The mean surface compositions were evaluated from 10 random measurements

over the material surface, where each measurement location covered an area of 65×45 μm^2.

Back-Scattered Electron (BSE) images were taken from polished sample cross-sections using

an FEI Nova NanoSEM 450 instrument at a beam acceleration voltage of 20 kV and spot size

of 5.5. Vickers indentation hardness was evaluated using a Struers Durascan® 70 hardness

tester. The indentation load and dwell time were 0.025 kg and 15 s, respectively. The mean

material surface hardness, $HV_{0.025}$, was averaged from 12 randomly-distributed indents.

Nanoindentation hardness measurements were performed on polished sample cross-sections

using a Hysitron TriboScope® Nanoindentor (≤5 mN load, Berkovich diamond indenter).

The displacements of indentations from the sample surface were measured in-situ using an

atomic force microscope attached to the nanoindentor. The mean hardness value at each

depth level was averaged from 5 indentations.

X-ray diffraction analysis was performed at two-theta angles from 30° to 80° in Bragg-

Brentano geometry using a Bruker D2 PHASER (30 kV, 10 mA, Cu-Kα_{ave} 0.1542 nm) and in

Seeman-Bohlin geometry at 2° Glancing Angle (GAXRD) using a PANalytical X′pert[3]

instrument (45 kV, 40 mA; monochromated CuKα_1 0.1541 nm). The 400°C 20hrs nitrided

and 450°C 20hrs nitrided Invar samples were also ground using P1200 SiC paper to

successively remove ~3/5/10/20/30 μm of treatment layer (measured using a micrometer) and

were examined respectively under GAXRD to determine the evolution of phase structure

with treatment depth. Cross-sectional thin foils for Transmission Electron Microscopy (TEM)

were prepared via Focused Ion Beam (FIB) milling using an FEI Quanta 200 3D electron

microscope with 30kV gallium ion beam attachment, as described previously [18]. The

thinned areas were examined under a Philips EM420 transmission electron microscope at a

140   beam acceleration voltage of 120 kV. Scanning TEM (STEM) analysis was carried out using

141   a FEI Philips Tecnai F20 electron microscope. STEM-EDX analysis was performed at 200

142   kV and a spot size of 6 (with Oxford Instruments AZtec EDX software).

143

144   **3   Results**

145   **3.1   Cross-sectional backscattered electron images and hardness-depth profiles**

146   All nitrided Invar 36 surfaces show a discontinuous, feature-containing surface layer in **Fig. 1**

147   (see **Appendix I** for BSE images of lower magnification). Neither the penetration depths nor

148   the distributions of these features on nitrided Invar are homogenous. At a treatment

149   temperature of 400°C, the dark features start forming from the very surface of material (**Fig.**

150   **1a**) and then grow and coalesce with treatment time (**Fig. 1d**). 'Cellular' regions are observed

151   in Invar 36 TPN-treated at 425°C and 450°C. These cellular regions are composed of

152   laminates of two different phases, with an interlamellar spacing of several tens of nanometers.

153   Owing to the large discrepancy in atomic mass between interstitial nitrogen atoms and

154   substitutional metal atoms (i.e. 14 for N, 55.8 for Fe and 58.7 for Ni), the features observed

155   on sample cross-sections of Invar 36 under backscattered electron (BSE) imaging (**Fig. 1**)

156   mainly originate from the inhomogeneous distribution of nitrogen following TPN treatment.

157   Under BSE imaging in **Fig. 1**, lower mean atomic weight yields less electron scattering, so

158   the N-rich phase appears dark (and will be identified in the following **Section 3.3**). It should

159   also be mentioned that the black wavy features (in **Fig. 1f**) are cracks and this feature is

160   clearly shown in the FIB-TEM sample in **Section 3.2**.

161
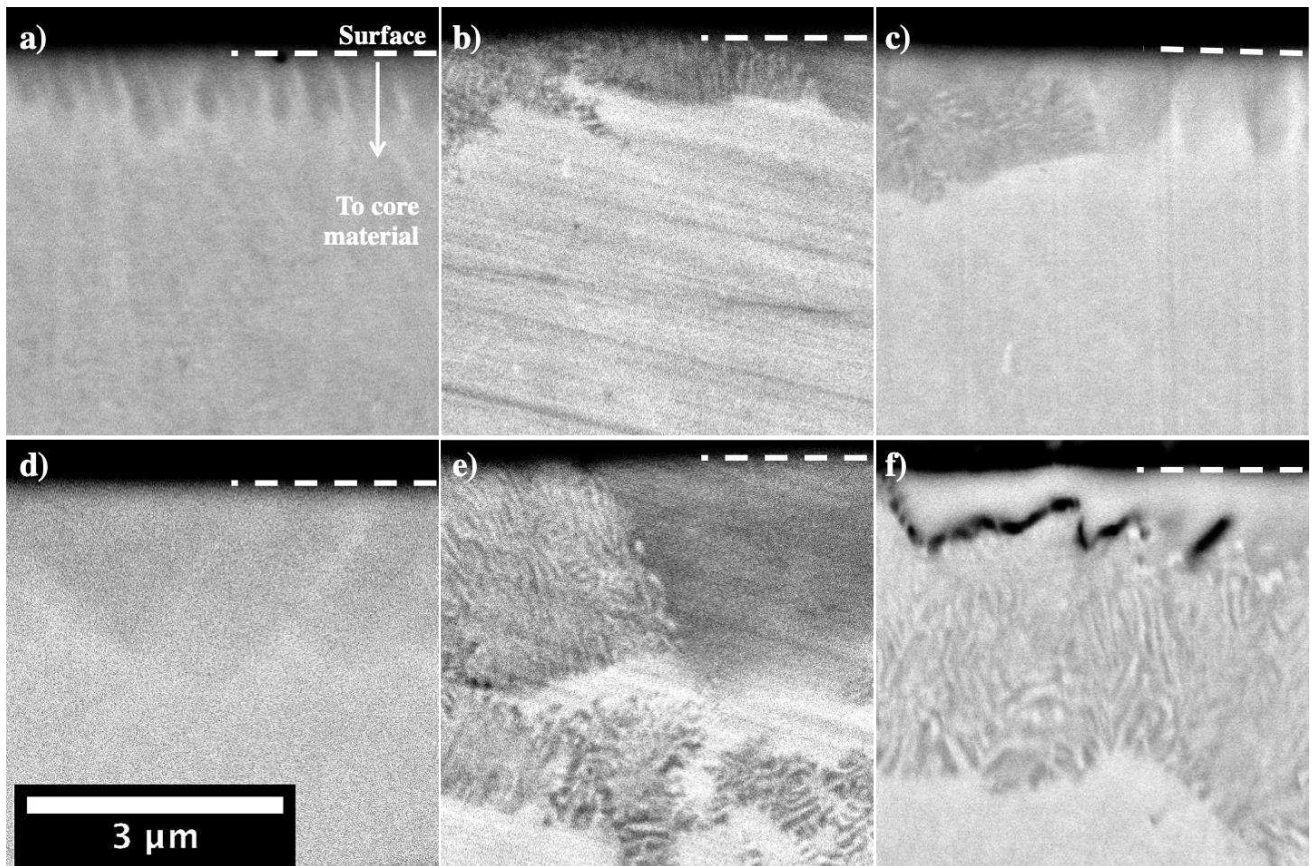
Fig. 1 Cross-sectional BSE images of Invar 36® after plasma nitriding at a) 400°C 4hrs, b) 425°C 4hrs, c) 450°C 4hrs, d) 400°C 20hrs, e) 425°C 20hrs, f) 450°C 20hrs

The hardness-depth profiles of nitrided Invar (**Fig. 2a**) indicate total case depths of ~11 μm and ~24 μm after treatments at 400°C and 450°C, respectively. Hardness profiles of nitrided Invar first drop steeply after leaving the nitride-containing surface layer and then gradually reduce as approaching towards core. The hardened layers on nitrided Invar are clearly thicker than the feature-containing layers (observed in BSE images, **Fig. 1d, f**) would suggest and correspond to deep nitrogen diffusion zones (see **Section 3.3**).

6
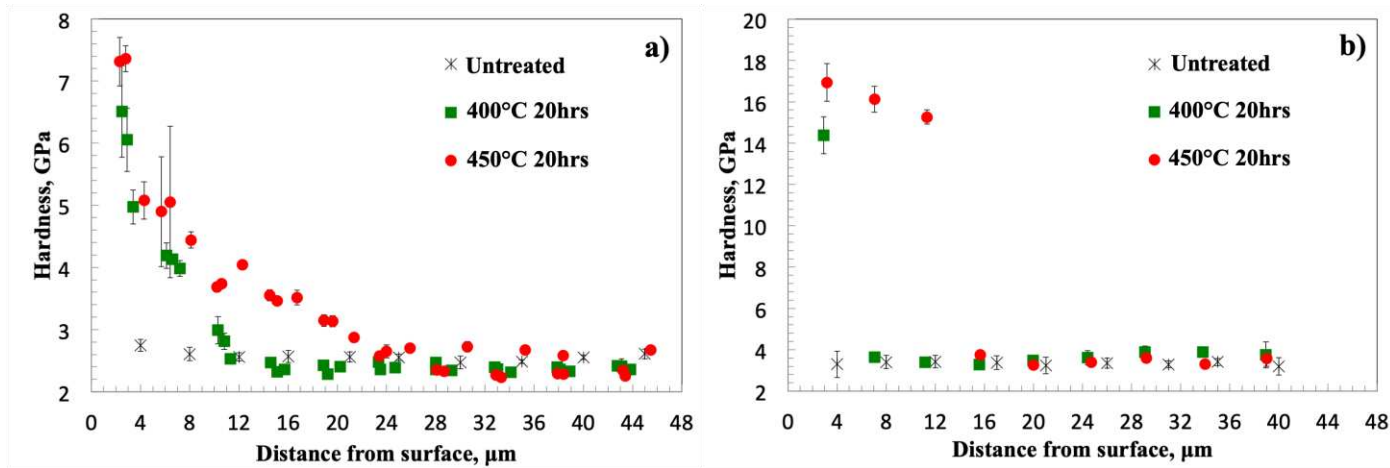
Fig. 2 Cross-sectional nanoindentation hardness-depth profiles of a) Invar 36® and b) RA 330® before and after TPN at 400°C and 450°C for 20hrs (error bars − ± 95% confidence interval at each depth level)

In contrast, homogenous γ_N-330 layers were observed on alloy RA 330 after equivalent nitriding treatments [18]. The hardened case depths on TPN-treated RA 330 in **Fig. 2b** are consistent with the observed layer depths, i.e. ~4 μm at 400°C and ~14 μm at 450°C [18]. Compared to the hardness-depth profile of nitrided Invar (**Fig. 2a**), γ_N-330 layers (synthesised under equivalent treatment conditions) are much harder (but significantly thinner) and present an abrupt drop in hardness at the layer/core interface (a characteristic feature of N-supersaturated austenite layers on stainless steel surfaces [22, 35]).

3.2   Phase identification
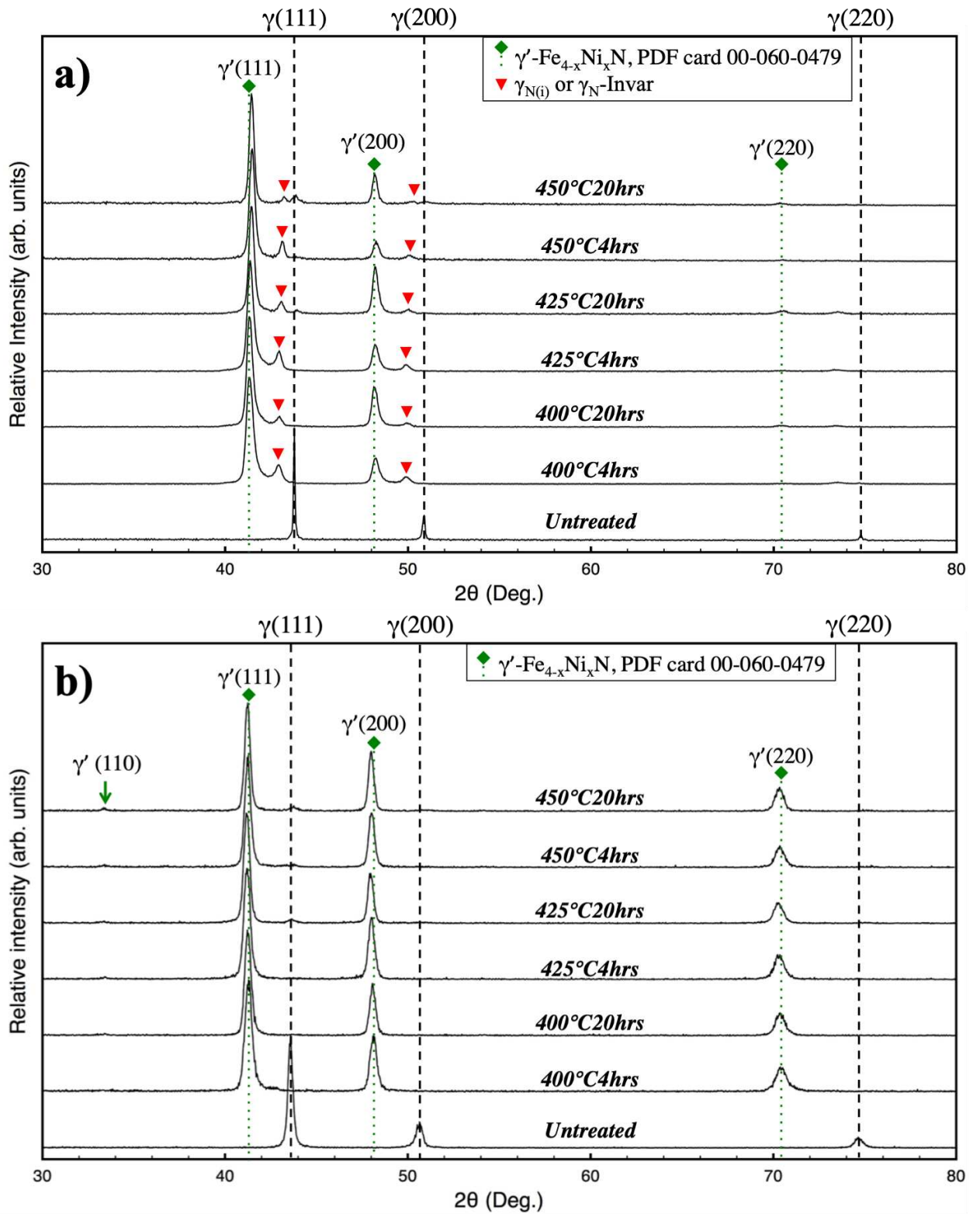
XRD and GAXRD

Fig. 3 a) Theta-2theta XRD and b) GAXRD profiles of TPN-treated Invar 36®

188
189
190
191

192   The XRD profiles of nitrided Invar 36 in **Fig. 3a** appear analogous to that reported for Invar

193   36 under nitrogen ion beam processing by Williamson et al. [29], showing "highly-expanded

194   and less-expanded FCC structures" after treatment − where both expanded structures have

195   almost ideal FCC structure (as determined from the 111 and 220 peak positions). Firstly,

196   under both θ-2θ XRD (**Fig. 3a**) and GAXRD (**Fig. 3b**), the peak positions of the 'highly-

197   expanded' FCC structure match with the $Fe_{4-x}Ni_xN$, PDF card 00-060-0479, stable for $0 < x <$

198   3.3 under experimental conditions [36]). This highly-expanded FCC structure (in **Fig. 3**)

199   could be identified as Fe_4N-type γ′-nitride. Different to the θ-2θ XRD profiles of TPN-treated

200   Invar (**Fig. 3a**), the GAXRD profiles of the same materials (**Fig. 3b**) reveal only the 'highly-

201   expanded FCC' phase (i.e. γ′-nitride) without the 'less-expanded' FCC phase. Considering

202   the shallow X-ray attenuation depth under GAXRD, γ′-nitride should correspond to a phase

203   located close to surface, with the 'less-expanded' phase formed deeper in the diffusion zone.

204   Then, the features observed in the near surface of nitrided Invar in **Fig. 1** can be attributed to

205   the formation of γ′-nitride. Additionally, an unexpanded γ(111) peak (near 43.5°) is also seen

206   on Invar after 20hrs treatment at 425°C and 450°C (**Fig. 3**), which could be correlates well

207   the (bright) N-depleted lamellae in 'cellular' region.

208

209   To reveal the surface phases on nitrided Invar (typically, the 'less-expanded FCC structure')

210   that contribute to deep hardened zones in **Fig. 2a**, the 400°C 20hrs and 450°C 20hrs nitrided

211   Invar samples were further investigated under GAXRD before and after successive layer

212   removal, as shown in **Fig. 4**. The γ′ peaks were observed on both samples to a depth of ~3

213   μm. At a depth of ~3 μm, unexpanded γ peaks are evident on Invar after TPN for 20hrs at

214   450°C, but are not observed after 20hrs treatment at 400°C. These unexpanded γ peaks at ~3

215   μm depth on the 450°C and 20hrs treated Invar alloy appear to correspond to the bright N-

216   depleted lamellar phase in the 'cellular' region in **Fig. 1f**.

217
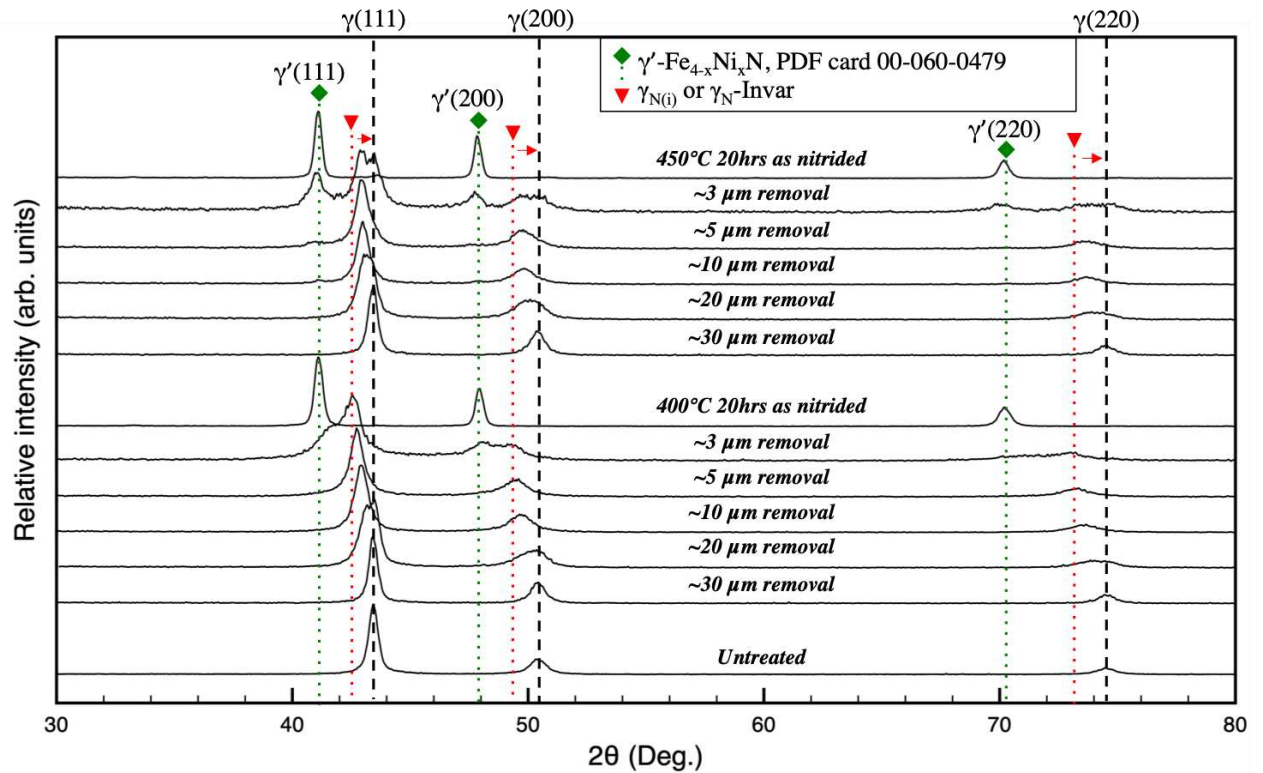
218
219 **Fig. 4** GAXRD profiles of the 400°C 20hrs and the 450°C 20hrs nitrided Invar 36® before

220 and after successive layer removal, as compared to the untreated sample

221

222 More importantly, below the γ′-containing surface zones, the 'less-expanded FCC structure'

223 is clearly revealed at depths from ~3 to 20 μm with continuous XRD peak shifts to higher 2θ

224 angles from surface to core (towards the peak positions of substrate austenite, as indicated by

225 red arrows in **Fig. 4**), until the unmodified core is reached at a depth of ~30 μm. The 'less-

226 expanded FCC structure', γ_N-Invar, appears to be continuously expanded from the parent

227 austenite under the insertion of interstitial nitrogen. The gradual shift of γ_N-Invar peaks to

228 higher 2θ angles with increasing depth could be attributed to the commensurate reduction of

229 nitrogen in solid solution from surface to core, which also leads to a gradually reducing
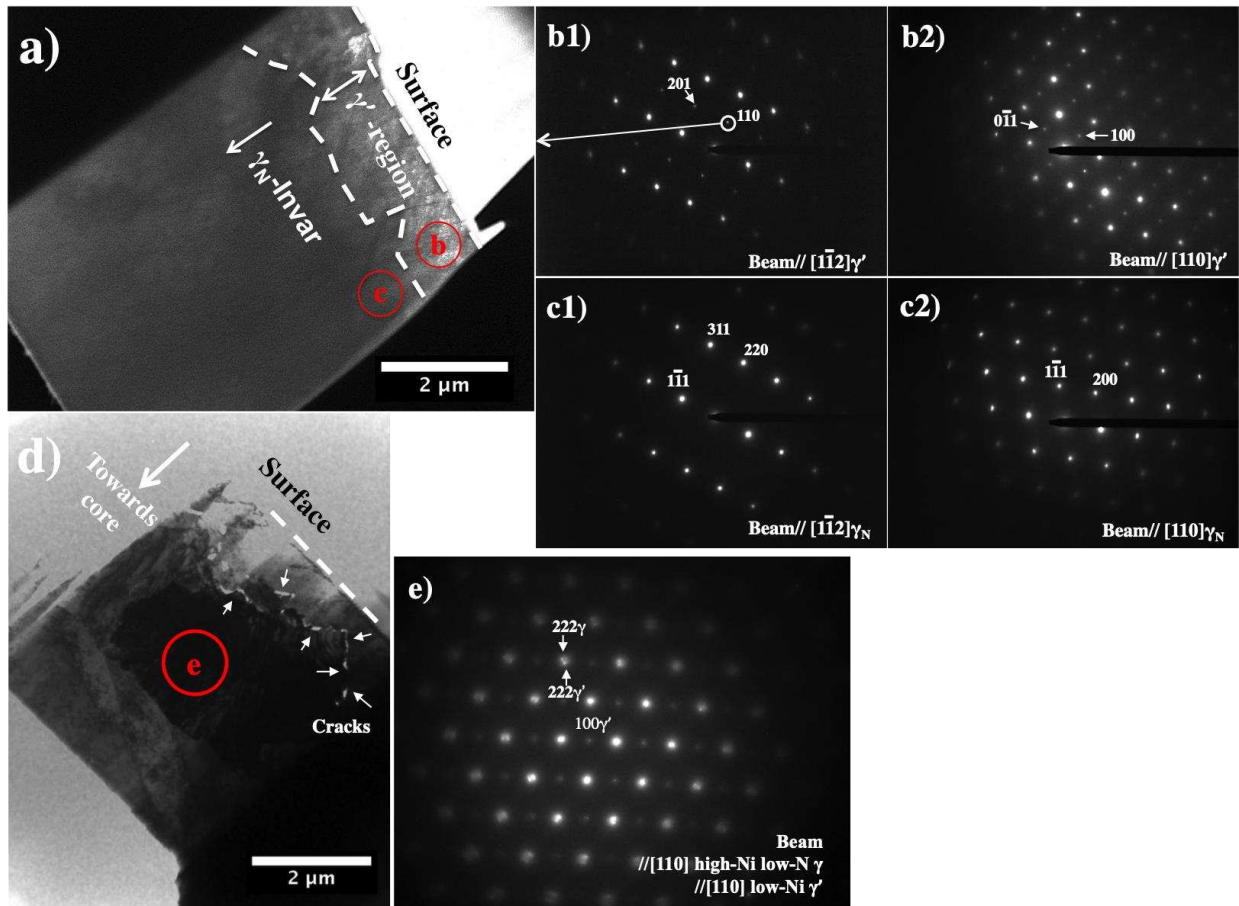
230 hardness with depth in the γ_N-Invar regions (**Fig. 2a**).

231

232 **FIB-TEM**

Fig. 5 a) DF-TEM image of 400°C 20hrs nitrided Invar, constructed with 110 γ′ diffraction

electrons as indicated in Fig. 6b1; b1,2) SAEDs of region b; c1,2) SAEDs of region c; d) BF-

TEM image of 450°C 20hrs nitrided Invar; e) SAEDs of region e

Cross-sectional TEM samples of 400°C and 450°C 20hrs nitrided Invar surfaces were also

prepared and investigated. Extra 'forbidden' FCC spots are revealed for γ′ (**Fig 5b1, 2** and

Fig. 5e), but not for γ_N-Invar (**Fig 5c1, 2**), in good agreement with the weak γ′(110) GAXRD

peaks observed in **Fig. 3b**. At a treatment temperature of 400°C, topmost γ′ is revealed under

DF-TEM imaging using γ′(110) diffraction electrons that γ′ appears slightly brighter than the

underlying γ_N-Invar (**Fig 5a**). This topmost γ′-nitride shares the same crystal orientation as

the underlying γ_N-Invar, with a cubic-to-cubic structure-orientation relationship, in which

case γ′ appears to be transformed from γ_N-Invar via interstitial-nitrogen ordering (into an

Fe_4N-type structure) during TPN.

11

247

There are different colonies of phase mixtures in the intermediate cellular regions on 450°C

and 20hrs TPN-treated Invar. The selected area EDP of a colony (i.e. the dark region in the

middle of **Fig. 5d**) presents two sets of FCC diffraction spots (**Fig. 5e**), suggesting a cubic-to-

cubic orientation relationship and a lattice parameter ratio of ~1.05 (as determined from

electron diffraction distances) between two phases. Taking one of the phases in the phase

mixture as being γ'-nitride (lattice parameter of 0.3789 nm, PDF card 00-060-0479), the

lattice parameter of the other FCC phase can be estimated as ~0.3609 nm, which is very close

to the lattice parameter of ~0.3606 nm measured for untreated austenite, as determined from

the 111 peak positions from GAXRD profiles in **Fig. 4**. Together with the γ' and unexpanded

XRD peaks observed for the 450°C TPN-treated Invar at ~3 μm depth in **Fig. 4**, the phase

mixture appears to be γ' and unexpanded γ. These colonies of phase mixtures do not share the

same crystal orientation to each other. No consistent crystallographic relation was observed

between the colony of phase mixture in **Fig. 5d** and the underlying (and probably the parent)

γ_N-Invar. The formation of these phase mixtures is likely to occur via nucleation and growth

of γ'. Additionally, cracks are observed and indicated with white arrows in **Fig. 5d**. These

micro-cracking are believed associated with the formation of γ'.

264

Furthermore, the lamellar phase mixture on Invar nitride at 450°C and 20hrs can clearly be

seen in HAADF imaging (**Fig. 6a**). STEM-EDX analysis of the phase mixture (**Fig. 6**)

indicates redistribution of both interstitial nitrogen and substitutional metallic elements (e.g.

Fe with Ni). Compared to the adjacent N-depleted regions, the N-rich regions exhibit higher

Fe content (**Fig. 6b**) but lower Ni content (**Fig. 6c**). Given that γ'-$Fe_{4-x}Ni_xN$ is stable for $0 < x$

< 3.3 [36], the γ' formed in cellular regions have different composition (i.e. much lower Ni

content) to those uniform γ' phases that formed via interstitial ordering (probably γ'-

272   Fe$_{2.6}$Ni$_{1.4}$N, at x ≈ 1.4 considering 35 at.% Ni). The high-Ni γ phase (adjacent to low-Ni γ′)

273   could still contain a very small amount of residual nitrogen, such that the γ phase in the

274   cellular region has a different composition to γ-Invar – and could therefore possess a different

275   lattice parameter. Thus, the phase mixture in cellular regions could be attributed to local

276   eutectoid decomposition of γ$_N$-Invar to an intimate mixture of lamellar low-Ni γ′ and high-Ni,

277   low-nitrogen γ. Additionally, minor alloying elements (such as Cr, Mn, Si, Co and C, see

278   **Table 1**) could also re-distribute between the two phases in this cellular region; however,

279   probably owing to their low concentrations, such re-distribution was not clearly visible in the

280   EDX analysis (see for example Cr in **Fig. 6e**).

281
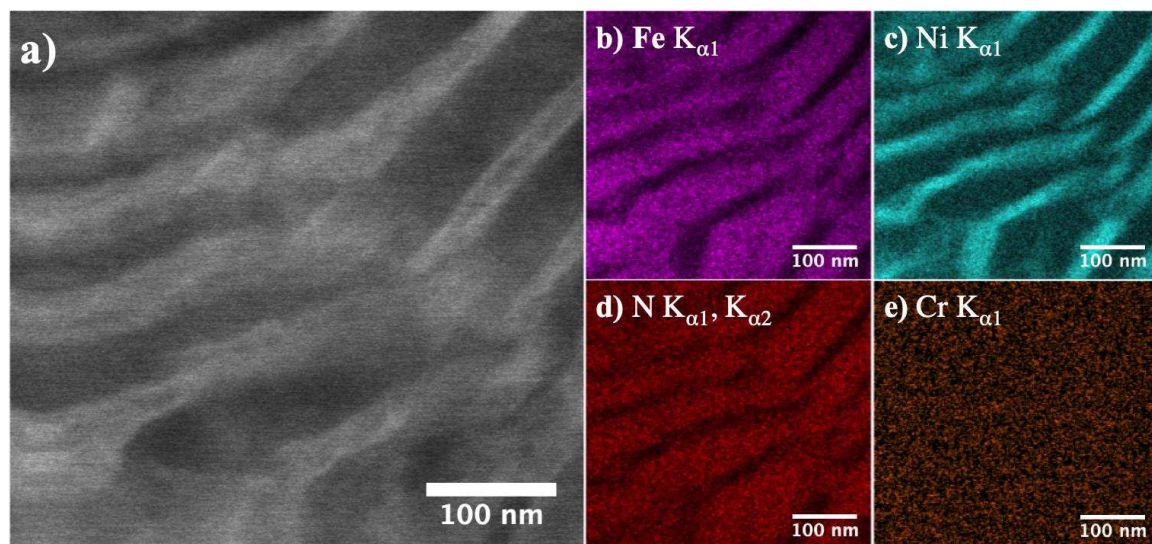
282

283   **Fig. 6** a) HAADF image showing the lamellar phase mixture, STEM-EDX maps of the

284   region for b) Fe (Kα1), c) Ni (Kα1), d) N (Kα1 and Kα2) and e) Cr (Kα1)

285

286   **3.3   Surface nitrogen content and hardness**

287   Surface nitrogen contents of nitrided Invar samples (**Table. 2**) ranged from ~18 to ~20 at.%,

288   which is significantly higher than the maximum equilibrium N-solubility limit in γ-Fe (i.e.

289   ~10.3 at.% at ~650°C [37]), but lower than the surface nitrogen content of the nitrided alloy

13

290   RA 330 (ranging from ~23 to 26 at.%) [18]. The presence of Cr in the austenitic lattice of

291   alloy RA 330 does appear to be beneficial in obtaining a higher surface nitrogen uptake.

292   Surface N content of Invar samples does not vary significantly with treatment temperature

293   and time, which could be attributed to the formation of γ' nitride at the substrate surface.

294

295   Both alloys exhibit significant hardening after TPN treatment (**Table. 2**) and the hardening

296   effect increases with treatment temperature and/or time. Maximum Vickers surface hardness

297   was achieved at the upper treatment condition (of 450°C for 20hrs) for both alloys. The

298   hardness values obtained are influenced by different factors, such as nitrogen composition-

299   depth profile, phase distribution, indent penetration depth and nitride layer depth. The

300   increase in surface hardness for TPN-treated Invar with treatment temperature and time could

301   be attributed to: i) the growth of a diffusion zone, ii) the development of uniform γ'-

302    $Fe_{2.6}Ni_{1.4}N$ phase at material surface, and iii) the lamellar phase mixtures that contain fine

303   lamella of low-Ni γ' and high-Ni (low-N) γ. Owing to the colossal nitrogen supersaturation,

304   alloy 330 generally possesses significantly higher surface hardness compared to Invar under

305   equivalent treatment conditions, although the nitrided layers on alloy 330 tend to be thinner

306   than those on Invar after an equivalent TPN treatment.

307

308   **4   Discussion**

309   **4.1   Interstitial nitrogen absorption and lattice expansion**

310   In this study, γ_N denotes the entire group of nitrogen-expanded austenites, with specific phase

311   notation based on the substrate material, such as γ_N-Invar, γ_N-330 and γ_N-316 (formed on

312   Invar 36, alloy RA 330 and AISI 316 ASS, respectively). Comparisons between the γ_N-Invar

313   in this study and the γ_N-330 in Ref. [18] reveal that a significant amount of Cr in the substrate

314   does appear to be conducive to obtaining extremely high levels of interstitial nitrogen

315 incorporation, but is at the same time not a necessity for the nitrogen-induced lattice

316 expansion phenomenon to occur. The γ_N-Invar observed could be classified as $\gamma_{N(i)}$ (i.e. where

317 (i) signifies an absence of strong-nitride-formers in the substrate alloy composition), while

318 the widely-reported interstitial nitrogen-supersaturated and (typically strongly anisotropic)

319 expanded austenite synthesised on Cr-containing ASSs could be denoted as $\gamma_{N(ii)}$. Noticeably,

320 the commercial Invar 36® alloy employed in this study still contains ~0.7 wt.% Cr (and $\leq$

321 0.032 wt.% of Al + Mg + Ti + Zr, see **Table 1**), while the Invar steel substrate used in Ref.

322 [29] (where γ_N-Invar was also synthesised) was reported to contain minor Si content (i.e. ~ 1

323 at.% of Mn + Si + C).

324

325 The terminology of "expanded austenite" was originally introduced to describe austenites

326 with expanded lattice parameters (after nitriding treatments), over those for nitrogen-

327 containing austenite at maximum equilibrium solubility [38]. After the re-definition of

328 "heavily strained austenite" for this terminology [3], expanded austenite are typically used to

329 denote the interstitially-supersaturated (and anisotropically expanded) austenites generally

330 investigated and reported in the field of Surface Engineering [39]. Nevertheless, expanded

331 austenite, taking the literal meaning of the terminology, includes both $\gamma_{N(i)}$ and $\gamma_{N(ii)}$. With

332 there being no (or much lower amounts of) "nitrogen-trappers" in γ_N-Invar, the route by

333 which $\gamma_{N(i)}$ forms appears to be different to the "nitrogen-trapping" in $\gamma_{N(ii)}$. The ability to

334 accommodate interstitial nitrogen in the parent FCC matrix (with a lattice expansion)

335 typically at non-equilibrium conditions (i.e. low treatment temperatures) arguably depends on

336 the 'chemical environment' (or, as suggested by Dong [22], the electronic structure) provided

337 by the parent alloy with respect to the interstitial species (e.g. N or C atoms), rather than

338 simply the presence of a significant amount of Cr (or another strong-nitride-former).

339

340   Interstitial supersaturation is a known (and probably the most essential) feature for $\gamma_{N(ii)}$. As

341   for γ_N-Invar, there is a lack of information on the equilibrium N solubility in γ-Invar and it is

342   still a question, as to whether the γ_N-Invar obtained is N-supersaturated or dissolves nitrogen

343   below the equilibrium solubility limit. Nitrogen solubility in Fe-Ni alloys is known to

344   decease as Ni content increases [40]. According to the partial isothermal section of Fe-Ni-N

345   at 700°C [36], the equilibrium nitrogen solubility drop from ~10 at.% in γ-Fe to ~1 at.% in γ-

346   (Fe, 35Ni). Thus, it is anticipated that the equilibrium nitrogen solubility in γ-Invar will be

347   much lower than that in 'pure' γ-Fe (i.e. ~10.3 at.% N at ~650°C [37]). Nevertheless, the

348   lattice parameters for γ_N-Invar (~0.364 nm at 450°C and up to ~0.368 nm at 400°C, measured

349   from the 111 γ_N-Invar peak positions at ~3 μm depth in **Fig. 4**) are very close to that of γ-Fe

350   with nitrogen at maximum equilibrium solubility (estimated as ~0.365 nm, using $0.3572\ +$

351     $[0.00078\ \times\ at.\%N]$ from Ref. [41]). Given such substantial lattice expansion, the γ_N-Invar

352   obtained is likely N-supersaturated (and could be metastable). However, further study is still

353   required to establish precisely the chemical composition (especially the upper limit of

354   nitrogen solvation) of γ_N-Invar and to understand the thermodynamic properties of Fe-Ni-N,

355   typically with Ni content close to ~35 at.% Ni and at temperatures below 450°C.

356

357   Owing to the different interstitial absorption, one other significant difference between $\gamma_{N(i)}$

358   and $\gamma_{N(ii)}$ are their lattice expansions observable under XRD. The XRD peak shifts (to lower

359   2θ angles, with respect to substrate peak positions) of γ_N-Invar are much smaller than those of

360   γ_N-330 after equivalent thermochemical treatments. More importantly, anomalous

361   (anisotropic) lattice expansion, where the XRD peak shift appears significantly larger for 200

362   reflections than with other hkl planes, is a known signature for the $\gamma_{N(ii)}$ synthesised on ASSs

363   under low-temperature nitriding [7, 11, 17] (as observed also for γ_N-330 [18]). In comparison

364   to $\gamma_{N(ii)}$, γ_N-Invar exhibits an seemingly 'isotropic' lattice expansion − where the observed

365 111 and 200 XRD peak shifts appear similar after nitrogen-insertion (**Fig. 3**) − for non-

366 stainless austenitic steels under low-temperature nitrogen diffusion treatment. However,

367 taking the GAXRD peak positions (from **Fig. 4**) of substrate γ-Invar and the γ_N-Invar at a

368 depth of ~5 μm, the lattice expansions measured for the 111 and 200 XRD reflections are i)

369 ~1.6% and ~1.8%, respectively, at 400°C and 20hrs, and ii) ~1.1% and ~1.2%, respectively,

370 at 450°C and 20hrs. γ_N-Invar also deviates from an ideal FCC structure, but such deviation

371 appears much less pronounced for γ_N-Invar, presumably owing to the much lower nitrogen

372 absorption levels. Such "slightly distorted FCC structure" of γ_N-Invar could be attributed

373 mainly to the effect of elastic anisotropy of the FCC lattice (with a small compressive stress

374 state) under N-induced lattice expansion. The γ_N-Invar layer synthesised under ion

375 implantation for 15 mins by Williamson et al. [29] is much thinner than the γ_N-Invar layers

376 synthesised under TPN in this study, where the θ-2θ XRD profile of the former covers the

377 entire γ_N-Invar layer and the abovementioned expansion anisotropy was not clearly observed.

378 Furthermore, an "expanded FCC" phase was reported on alloy 330 after hot ammonia

379 corrosion at 500°C for 1540hrs [42], which was presumed as a nitrogen-containing iron-

380 nickel phase (after the formation of Cr nitride) that may be a phase similar to γ_N-Invar.

381 However, given the white mono-layer shown in cross-section after etching and the absence of

382 CrN under XRD examination of the "corroded" alloy 330 [42], the "expanded FCC" phase on

383 alloy 330 is suspected to be γ_N-330, and probably therefore the first explicit example of $\gamma_{N(ii)}$

384 published in the open journal literature.

385

386 Last but not the least, the 'less expanded FCC structure' on Invar (Fe-35Ni, in [29]) can now

387 be identified as $\gamma_{N(i)}$, being a Cr-free N-expanded austenite. However, Ni-20Fe [29], Fe-30Ni,

388 Fe-32Ni, Fe-42Ni and some FCC Fe-Mn-C steels [19, 20] − as also having Cr-free FCC

389 substrate structure (based on Fe-Ni or Fe-Mn-C system) − showed only a thin γ' layer without

390      $\gamma_{N(i)}$ under low-temperature nitriding treatments (or nitrogen ion implantation). Nevertheless,

391   detailed structural/compositional information was not provided for the nitrided non-stainless

392   austenitic steels in Ref. [19, 20, 29]. There might be thick γ' surface layers, such that

393   underlying nitrogen-containing metallic phase(s) were not revealed by XRD. It may be

394   worthwhile to re-visit these alloys (typically the Fe-Ni binary steels with Ni content close to

395   ~35Ni wt.%) under low-temperature thermochemical diffusion treatments. If $\gamma_{N(i)}$ forms only

396   on certain substrate compositions, further study may be required on the electronic structure,

397   bonding states and/or the magnetic properties of γ_N-Invar to elucidate the mechanisms of its

398   formation.

399

400   **4.2   Decomposition of γ_N**

401   Given the cubic-to-cubic crystallographic orientation relationship between γ' and γ_N-Invar

402   seen after nitriding at 400°C (**Fig. 5a-c**), the formation of Fe_4N-type γ' in γ_N-Invar could be

403   realised via diffusion and ordering of the interstitial nitrogen, without the need for

404   substitutional diffusion. At elevated treatment temperatures, eutectoid decomposition occurs

405   in γ_N-Invar under segregation of substitutional elements (**Fig. 6**). The cellular decomposition

406   morphology of γ_N-Invar appears similar to that of decomposed γ_N-316 [43]. Nevertheless,

407   decomposition products of γ_N-Invar in the cellular regions are Fe_4N-type $\gamma' + \gamma$, whereas for

408   γ_N-316 they are $CrN + \gamma$.

409

410   One signature feature of $\gamma_{N(ii)}$ is its metastability under paraequilibrium conditions, where the

411   low diffusivity of substitutional elements (e.g. Fe, Cr and Ni) hinders the lattice

412   decomposition mechanisms associated with CrN formation. After TPN at 400°C, no evidence

413   of CrN was found in γ_N-330 [18], whereas γ' forms in γ_N-Invar via interstitial ordering. At

414   slightly higher treatment temperatures (i.e. 425°C and 450°C), the substitutional-diffusion

415   facilitated decomposition occurs more readily in Cr-free γ_N-Invar, compared to γ_N-330.

416   Although $\gamma_{N(i)}$ (e.g. γ_N-Invar) may exhibit significantly lower nitrogen solvency and lattice

417   expansion than $\gamma_{N(ii)}$ (e.g. γ_N-330), the former appears thermodynamically less stable. In this

418   case, Cr atoms in $\gamma_{N(ii)}$ assist in stabilising the N-rich and expanded FCC structure, by i)

419   providing Cr-N type bonding that competes with the Fe-N type bonding, and ii) providing an

420   extremely slow lattice decomposition mechanism at the low treatment temperatures

421   employed. Future investigations could be performed to address the as yet unanswered

422   questions, as to i) how much "nitrogen-trapper" is required in the substrate alloy composition

423   for the onset of $\gamma_{N(ii)}$ formation after thermochemical diffusion treatment, and ii) whether

424   other strong nitride forming elements could replicate the role of (or replace) Cr in obtaining

425    $\gamma_{N(ii)}$ on austenitic steel substrates. Furthermore, addition of strong nitride forming elements

426   other than Cr could inhibit the formation of CrN in $\gamma_{N(ii)}$ and push the thermal stability of $\gamma_{N(ii)}$

427   to a higher treatment temperature [44], in which case austenitic metallic substrates alloyed

428   with combinations of strong-nitride forming elements (e.g. Cr, Al, Ti and/or Nb; each

429   element to no more than a few weight percent) may possess superior thermodynamic stability

430   upon nitrogen supersaturation, enabling higher treatment/service temperature of nitrogen-

431   expanded austenite.

432

4.3   Nitrogen interstitial diffusion

434   Comparing the surface nitrogen contents and the hardness-depth profiles between Invar 36

435   (**Fig. 2a**) and alloy RA 330 (**Fig. 2b**) after TPN treatment, nitrogen atoms were retained at the

436   surface and distributed more homogenously in the relatively thin diffusion layers of $\gamma_{N(ii)}$.

437   However, the high level of Cr content in stainless steel substrates, whilst promoting lattice

438   interstitial supersaturation (and thus superior hardening response), appears also to impede

439   significantly nitrogen inward diffusion, possibly owing to the trapping and detrapping

440   diffusion kinetics proposed in [26]. Noticeably, the Invar 36 substrate contains minor

441   additions of strong nitride formers (e.g. Cr, Al, Ti and Zr, in total below ~0.1 wt.%), which

442   could influence the nitrogen diffusion rate in Invar 36. There should be a threshold

443   concentration level of the strong nitride former (or combinations thereof) in austenitic steel,

444   above which interstitial diffusion in the austenite matrix slows down and nitrogen atoms are

445   retained at the surface owing to the 'trap effect'.

446

447   Comparing thermochemical diffusion treatments of AISI 316 ASS by nitrogen (γ_N-316) or

448   carbon (γ_C-316) in literature (the alloy for which probably the most extensive prior published

449   data exists), γ_N-316 layers possess composition-depth profiles with a high nitrogen plateau

450   followed an abrupt drop in nitrogen content at the diffusion layer front (with corresponding

451   lattice expansions and hardness/depth profiles) [35, 45, 46], while the carbon concentration

452   (and corresponding lattice expansion and hardness) in γ_C-316 layers is normally lower and

453   with a smoothly-reducing depth profile towards the substrate core [8, 45-47]. As for the

454   chemically-homogenous γ_C-316 and γ_N-316 powders, carbon absorption of γ_C-316 ranges

455   from 0 to ~18 at.% [48, 49], while γ_N-316 has been shown to possess a lower limit of

456   interstitial nitrogen solvation (e.g. ~14-38 at.% N [10]). For the γ_N-Invar zones observed in

457   this study, the continuous lattice expansion from the unmodified core (**Fig. 4**) and the

458   smoothly reducing hardness-depth profiles (**Fig. 2a**) hints at there being no lower interstitial

459   solvation limit – and the smoothly reducing nitrogen depth profile appears very different to

460   γ_N-316 (but somewhat similar to γ_C-316). The abovementioned differences between γ_N-316

461   (as a type of $\gamma_{N(ii)}$) and γ_N-Invar (as a type of $\gamma_{N(i)}$), which could be associated to the strong

462   chemical affinity between Cr and N, confirm the influence from the 'chemical environment'

463   of the substrate alloy (e.g. with or without Cr) on the absorption of interstitial N during

464   thermochemical diffusion treatments.

465

4.4   Nitrogen interstitial ordering

Compared to FCC-γ, one distinctive feature of γ' is the nitrogen interstitial ordering, where

the 'inserted' N atoms occupy the body centres, i.e. $\frac{1}{2} \frac{1}{2} \frac{1}{2}$, of the host FCC cubes. Such

interstitial ordering give rise to the extra 'forbidden' FCC reflections in EDPs (compare **Fig.**

5b1-2 and **Fig. 5c1-2**) and the $\gamma'(110)$ peak under XRD (**Fig. 3b**). These extra diffraction

reflections are also widely observed for $\gamma_{N(ii)}$ layers, reported under both electron diffraction

(e.g. in γ_N-316 [50, 51], γ_N-304 [52] and γ_N-AG17 [18]) and XRD (i.e. γ_N-316 [53]). These

reflections are not observed in $\gamma_{N(ii)}$ when nitrogen content is low [18, 51] and are only

observed under XRD when the nitrogen content is extremely high (i.e. for the 'chemically-

homogenous' γ_N-316 powders containing ~35.5 at.% N [53]). With increasing nitrogen

content, $\gamma_{N(ii)}$ could show i) no forbidden FCC reflections (at low N content), ii) forbidden

reflections under electron diffraction (potentially owing to nitrogen-interstitial ordered

domains [51] at intermediate-to-high N content), and iii) forbidden reflections under X-ray

diffraction (owing to long-range ordering of interstitial nitrogen [53] under extreme

conditions of high N uptake). More importantly, Cr-containing Fe_4N-like γ' phases [54] were

reported in the $\gamma_{N(ii)}$ formed on Fe-Cr-Ni alloys, typically at the topmost surface (with the

highest nitrogen concentration). The Cr-containing Fe_4N-like γ' in $\gamma_{N(ii)}$ is somewhat

comparable to the uniform Cr-free Fe_4N-type γ' in $\gamma_{N(i)}$, that both of them could form via

interstitial diffusion and/or ordering of nitrogen at low treatment temperature. In this regard,

$\gamma_{N(ii)}$ could exhibit either a random solid solution of N, short-range-ordering of N or long-

range-ordering of N, depending on the local nitrogen concentration. The exact position of N

in $\gamma_{N(ii)}$ is so far unclear and should vary at different stages of nitrogen absorption level, but it

is most likely that N atoms are 'trapped' at octahedral interstices near substitutional Cr atoms

in the FCC unit cell. In contrast, the $\gamma_{N(i)}$ in this study does not present extra 'forbidden'

490   diffraction signals either under electron diffraction nor by XRD, i.e. there is no evidence of

491   any interstitial ordering. A Fe-Ni-N solid solution is anticipated for $\gamma_{N(i)}$, with nitrogen atoms

492   occupying randomly some fraction of the octahedral interstices.

493

494   **Conclusions**

495   Further to a previous study on the role of Mn and Ni in the formation and structure of

496   nitrogen-expanded austenite on ASSs, another (and arguably more important) aspect, on the

497   role of Cr in the formation of γ_N (and/or on the alloy selection/design criteria for nitrogen

498   interstitially-expandable steels/alloys), is discussed in present work. Comparing to the

499   anisotropic nitrogen-expanded austenite $\gamma_{N(ii)}$ (e.g. γ_N-330 that formed on 330 alloy), an

500   almost isotropic nitrogen-expanded austenite $\gamma_{N(i)}$ (viz. γ_N-Invar) is revealed on a non-

501   stainless austenitic steel (Invar 36®) after TPN treatment, showing very different lattice

502   expansion and surface hardening behaviour. Cr-alloying in austenitic steel substrates is an

503   important factor in obtaining colossal nitrogen interstitial supersaturation; but the occurrence

504   of interstitial-induced lattice expansion under low temperature nitrogen thermochemical

505   diffusion treatment does not required a significant content of Cr in substrate.

506

507   The γ_N-Invar diffusion zones, although providing less of a hardening effect, are much thicker

508   than those on γ_N-330. Comparing the decomposition between γ_N-330 and γ_N-Invar, the

509   presence of Cr-alloying appears beneficial in suppressing the formation of γ'-Fe_4N type iron

510   nitrides and enhancing the thermodynamic stability of γ_N. This implies a need for further

511   study on the contents of nitride-forming elements required in austenitic alloys (or austenite-

512   containing duplex or precipitation-hardening alloy) to effectively 'trap' interstitial N atoms

513   for optimum nitrogen absorption during low-temperature diffusion treatment (i.e. to

514   maximise – and stabilise – γ_N formation, whilst retaining high nitrogen interstitial inward

515   diffusion rates for hard and thick treatment layers). For example, austenitic metallic matrices

516   (e.g. Ni or Fe-Ni/Mn) alloyed with (combinations of) strong nitride-forming elements could

517   be evaluated under different low-temperature nitriding conditions, to explore the optimal

518   balance between treatment efficiency and treatment layer stability.

519

524 **References**

525 [1] Z.L. Zhang, T. Bell, Structure and corrosion resistance of plasma nitrided stainless
526 steel, Surf. Eng. 1(2) (1985) 131-136.
527 [2] K. Ichii, K. Fujimura, T. Takase, Structure of the ion-nitrided layer of 18-8
528 stainless steel, Technology Reports of Kansai University 27 (1986) 135-144.
529 [3] A. Leyland, D.B. Lewis, P.R. Stevenson, A. Matthews, Low temperature plasma
530 diffusion treatment of stainless steels for improved wear resistance, Surf. Coat.
531 Technol. 62 (1993) 608-617.
532 [4] D.B. Lewis, A. Leyland, P.R. Stevenson, J. Cawley, A. Matthews, Metallurgical
533 study of low-temperature plasma carbon diffusion treatments for stainless steels, Surf.
534 Coat. Technol. 60 (1993) 416-423.
535 [5] A. Matthews, A. Leyland, Plasma processing for enhanced wear and corrosion
536 performance, Mater. Sci. Forum 163-165 (1994) 497-508.
537 [6] Y. Sun, T. Bell, Sliding wear characteristics of low temperature plasma nitrided
538 316 austenitic stainless steel, Wear 218 (1998) 31-42.
539 [7] Y. Sun, X.Y. Li, T. Bell, X-ray diffraction characterisation of low temperature
540 plasma nitrided austenitic stainless steels, J. Mater. Sci. 34 (1999) 4793-4802.
541 [8] Y. Cao, F. Ernst, G.M. Michal, Colossal carbon supersaturation in austenitic
542 stainless steels carburized at low temperature, Acta Mater. 51 (2003) 4171-4181.
543 [9] S. Collins, P. Williams, Low-temperature colossal supersaturation, Advanced
544 Materials and Process, ASM International, 2006, pp. 32-33.
545 [10] T. Christiansen, M.A.J. Somers, Controlled dissolution of colossal quantities of
546 nitrogen in stainless steel, Metall. Mater. Trans. A 37A (2006) 675-682.
547 [11] T. Christiansen, M.A.J. Somers, On the crystallographic structure of S-phase, Scr.
548 Mater. 50 (2004) 35-37.
549 [12] T. Christiansen, M.A.J. Somers, Decomposition kinetics of expanded austenite
550 with high nitrogen contents, Z. Metallkd. 97(1) (2006) 79-88.
551 [13] J. Buhagiar, X. Li, H. Dong, Formation and microstructural characterisation of S-
552 phase layers in Ni-free austenitic stainless steels by low-temperature plasma surface
553 alloying, Surf. Coat. Technol. 204(3) (2009) 330-335.
554 [14] J.C. Stinville, P. Villechaise, C. Templier, J.P. Riviere, M. Drouet, Lattice
555 rotation induced by plasma nitridng in a 316L polycrystalline stainless steel, Acta
556 Mater. 58 (2010) 2814-2821.
557 [15] C. Templier, J.C. Stinville, P. Villechaise, P.O. Renault, G. Abrasonis, J.P.
558 Riviere, A. Martinavicius, M. Drouet, On lattice plane rotation and crystallographic
559 structure of the expanded austenite in plasma nitrided AISI 316L steel Surf. Coat.
560 Technol. 204 (2010) 2551-2558.
561 [16] F.A.P. Fernandes, T.L. Christiansen, G. Winther, M.A.J. Somers, On the
562 determination of stress profiles in expanded austenite by grazing incidence X-ray
563 diffraction and successive layer removal, Acta Mater. 94 (2015) 271-280.
564 [17] B.K. Brink, K. Stahl, T.L. Christiansen, J. Oddershede, G. Winthiner, M.A.J.
565 Somers, On the elusive crystal structure of expanded austenite, Scr. Mater. 131 (2017)
566 59-62.
567 [18] X. Tao, X. Liu, A. Matthews, A. Leyland, The influence of stacking fault energy
568 on plasticity mechanisms in triode-plasma nitrided austenitic stainless steels:
569 Implications for the structure and stability of nitrogen-expanded austenite, Acta Mater.
570 164 (2019) 60-75.
571 [19] E. Menthe, K.T. Rie, J.W. Schultze, S. Simsson, Structure and properties of
572 plasma-nitrided stainless steel, Surf. Coat. Technol. 74-75 (1995) 412-416.

573 [20] N. Yasumaru, Low-temperature ion nitriding of austenitic stainless steels,
574 Materials Transactions - The Japanese Institute of Metals 39 (1998) 1046-1052.
575 [21] D.L. Williamson, I. Ivanov, R. Wei, P.J. Wilbur, Role of Chromium in high-dose,
576 high rate, elevated tempearture nitrogen implantation of austenitic stainless steels,
577 Material Research Society Symposium Proceedings 235(473-478) (1992).
578 [22] H. Dong, S-phase surface engineering of Fe-Cr, Co-Cr and Ni-Cr alloys, Int.
579 Mater. Rev. 55(2) (2010) 65-98.
580 [23] R.B. Frandsen, T. Christiansen, M.A.J. Somers, Simutaneous surface engineering
581 and bulk hardening of precipitation hardening stainless steel, Surf. Coat. Technol. 200
582 (2006) 5160-5169.
583 [24] J. Lutz, J.W. Gerlach, S. Mandl, PIII nitriding of fcc-alloys containing Ni and Cr,
584 Physica Status Solidi A 205(4) (2008) 980-984.
585 [25] D.L. Williamson, J.A. Davis, P.J. Wilbur, J.J. Vajo, R. Wei, J.N. Matossian,
586 Relative roles of ion energy, ion flux, and sample temperature in low-energy nitrogen
587 ion implantation of Fe-Cr-Ni stainless steel, Nuclear Instruments and Methods in
588 Physics Research B 127/128 (1997) 930-934.
589 [26] S. Parascandola, W. Moller, D.L. Williamson, The nitrogen transport in
590 austenitic stainless steel at moderate temperature, Appl. Phys. Lett. 76 (2000) 2194-
591 2196.
592 [27] J.P. Riviere, M. Cahoreau, P. Meheust, Chemical bonding of nitrogen in low
593 energy high flux implanted austenitic stainless steel, J. Appl. Phys. 91(10) (2002)
594 6361-6366.
595 [28] J. Oddershede, T.L. Christiansen, K. Stahl, M.A.J. Somers, Extended X-ray
596 absorption fine structure investigation of nitrogen stabilized expanded austenite, Scr.
597 Mater. 62 (2010) 290-293.
598 [29] D.L. Williamson, J.A. Davis, P.J. Wilbur, Effect of austenitic stainless steel
599 composition on low-energy, high-flux nitrogen ion beam processing, Surf. Coat.
600 Technol. 103-104 (1998) 178-184.
601 [30] F. Pedraza, C. Savall, G. Abrasonis, J.P. Riviere, J.F. Dinhut, J.L. Grosseau-
602 Poussard, Low energy, high-flux nitridation of face-centred cubic metallic matrices,
603 Thin Solid Films 515 (2007) 3661-3669.
604 [31] T. Makishi, K. Nakata, Surface hardening of nickel alloys by means of plasma
605 nitriding, Metall. Mater. Trans. A 35A (2004) 227-238.
606 [32] M. Fonovic, A. Leineweber, O. Robach, A. Jagle, E.J. Mittemeijer, The nature
607 and origin of "double expanded austenite" in Ni-based Ni-Ti alloys developing upon
608 low temperature gaseous nitriding, Metall. Mater. Trans. A 46A (2015) 4115.
609 [33] A. Leyland, K.S. Fancey, A.S. James, A. Matthews, Enhanced plasma nitriding
610 at low pressures: a comparative study of d.c. and r.f. techniques, Surf. Coat. Technol.
611 41 (1990) 295-304.
612 [34] A. Leyland, K.S. Fancey, A. Matthews, Plasma nitriding in a low pressure triode
613 discharge to provide improvements in adhesion and load support for wear resistant
614 coatings, Surf. Coat. Technol. 7(3) (1991) 207-215.
615 [35] M.A.J. Somers, T. Christiansen, Gaseous processes for low temperature surface
616 hardening of stainless steel, in: E.J. Mittemeijer, M.A.J. Somers (Eds.),
617 Thermochemical Surface Engineering of Steels, Woodhead Publishing, Cambridge,
618 2015, pp. 581-614.
619 [36] P. Perrot, Iron - Nitrogen - Nickel, in: G. Effenberg, S. Ilyenko (Eds.), Landolt-
620 Bornstein - Group IV Physical Chemistry (Numerical Data and Functional
621 Relationships in Science and Technology), Vol. 11D, Part 4, Springer, Berlin,
622 Heidelberg, 2008.

[37] H.A. Wriedt, N.A. Gokcen, R.H. Nafziger, The Fe-N (iron-nitrogen) system, Bulletin of Alloy Phase Diagrams 8 (1987) 355.

[38] S.P. Hannula, O. Nenonen, Surface structure and properties of ion-nitrided austenic stainless steels, Thin Solid Films 181 (1989) 343-350.

[39] M.A.J. Somers, T. Christiansen, Low temperature surface hardening of stainless steel in: E.J. Mittemeijer, M.A.J. Somers (Eds.), Thermochemical Surface Engineering of Steels, Woodhead Publishing, Cambridge, 2015, pp. 557-579.

[40] D. Atkinson, C. Bodsworth, Thermodynamic proeprties of nitrogen in austenitic iron and iron-nickel alloys, J. Iron Steel Inst 208 (1970) 587-593.

[41] D. H. Jack, K.H. Jack, Invited review: Carbides and nitrides in steel, Materials Science and Engineering 11 (1973) 1-27.

[42] J.J. Moran, J.R. Mihalisin, E.N. Skinner, Behavior of stainless steels and other engineering alloys in hot ammonia atmospheres, Corrosion 17(4) (1961) 191t-195t.

[43] X.Y. Li, Y. Sun, Transmission electron microscopy study of S phase in low temperature plasma nitrided 316 stainless steel, in: T. Bell, K. Akamatsu (Eds.), Stainless Steel 2000: Thermochemical Surface Engineering of Stainless Steel, Maney Publishing, London, 2001.

[44] T. Christiansen, K.L. Dahm, M.A.J. Somers, New stainless steel alloys for low temperature surface hardening, BHM Berg- und Hüttenmännische Monatshefte 160(9) (2015) 406-412.

[45] T. Christiansen, M.A.J. Somers, Low temperature gaseous nitriding and carburising of stainless steel, Surf. Eng. 21 (2005) 445-455.

[46] S. Thaiwatthana, X.Y. Li, H. Dong, T. Bell, Comparison studies on properties of nitrogen and carbon S phase on low temperature plasma alloyed AISI 316 stainless steel, Surf. Eng. 18(6) (2002) 433-437.

[47] G.M. Michal, F. Ernst, H. Kahn, Y. Cao, F. Oba, N. Agarwal, A.H. Heuer, Carbon supersaturation due to paraequilibrium carburization: Stainless steels with greatly improved mechanical properties, Acta Mater. 54 (2006) 1597-1606.

[48] T.L. Christiansen, K. Stahl, B.K. Brink, M.A.J. Somers, On the carbon solubility in expanded austenite and formation of Hagg carbide in AISI 316 stainless steel, Steel Res. Int. 87(11) (2016) 1395-1405.

[49] T.S. Hummelshoj, T.L. Christiansen, M.A.J. Somers, Lattice expansion of carbon-stabilized expanded austenite, Scr. Mater. 63 (2010) 761-763.

[50] D. Stroz, M. Psoda, TEM studies of plasma nitrided austenitic stainless steel, J. Microsc. 237 (2010) 227-231.

[51] J.C. Jiang, E.I. Meletis, Microstructure of the nitride layer of AISI 316 stainless steel produced by intensified plasma assisted processing, J. Appl. Phys. 88(7) (2000) 4026-4031.

[52] K. Tong, F. Ye, H. Che, M.K. Lei, S. Miao, C. Zhang, High-density stacking faults in a supersaturated nitrided layer on austenitic stainless steel, J. Appl. Crystallogr. 49 (2016) 1967-1971.

[53] B.K. Brink, K. Stahl, T. Christiansen, C. Frandsen, M.F. Hansen, M.A.J. Somers, Composition-dependent variation of magnetic properties and interstitial ordering in homogenous expanded austenite, Acta Mater. 106 (2016) 32-39.

[54] H.L. Che, S. Tong, K.S. Wang, M.K. Lei, M.A.J. Somers, Co-existence of γ'N phase and γN phase on nitrided austenitic Fe-Cr-Ni alloys – I. experiment, Acta Mater. 177 (2019) 35-45.

672 **Tables**

673 **Table 1.** Material composition, in wt.%

Material	Specification	Fe	Cr	Ni	Mn	C	Others
Invar 36®[a]	ASTM F1686-06, UNS K93603	Bal.	0.07	36.08	0.4	0.04	0.14 Si, 0.04 Co
RA 330®[b]	ASTM B536-07 UNS N08330	Bal.	18.5	34.9	1.4	0.05	0.16 Al, 0.14 Ti, 0.11 Cu, 1.2 Si, 0.01N

674 [a]Composition of Invar 36® is presented according to the original material supplier

675 Deutsche Nickel Gmbh and it also contains 0.032 wt.% (in total) of minor alloying

676 additions of Al, Mg, Ti and Zr; The Ni content was confirmed using SEM-EDX.

677 [b]Composition of RA 330® is presented according to the original material supplier

678 ATI Allegheny Ludlum Corporation; the contents of major alloying elements (i.e. Cr,

679 Ni, Mn and Si) were confirmed using SEM-EDX.

680

681 **Table 2.** Surface nitrogen content and hardness

	Surface at.% Nitrogen	Surface hardness, $HV_{0.025}$	
	Invar 36®	Invar 36®	RA 330®
Untreated	/	200 ± 3	210 ± 4
400°C 4hrs	18.3 ± 0.4	390 ± 5	520 ± 10
400°C 20hrs	19.8 ± 0.3	498 ± 8	1048 ± 62
425°C4hrs	18.9 ± 0.3	531 ± 8	515 ± 17
425°C 20hrs	20.6 ± 0.3	705 ± 25	1494 ± 21
450°C 4hrs	18.8 ± 0.6	638 ± 8	786 ± 26
450°C 20hrs	19.6 ± 0.6	734 ± 12	1573 ± 18

682 *Values of surface nitrogen content and layer depths are shown as mean ± 95%

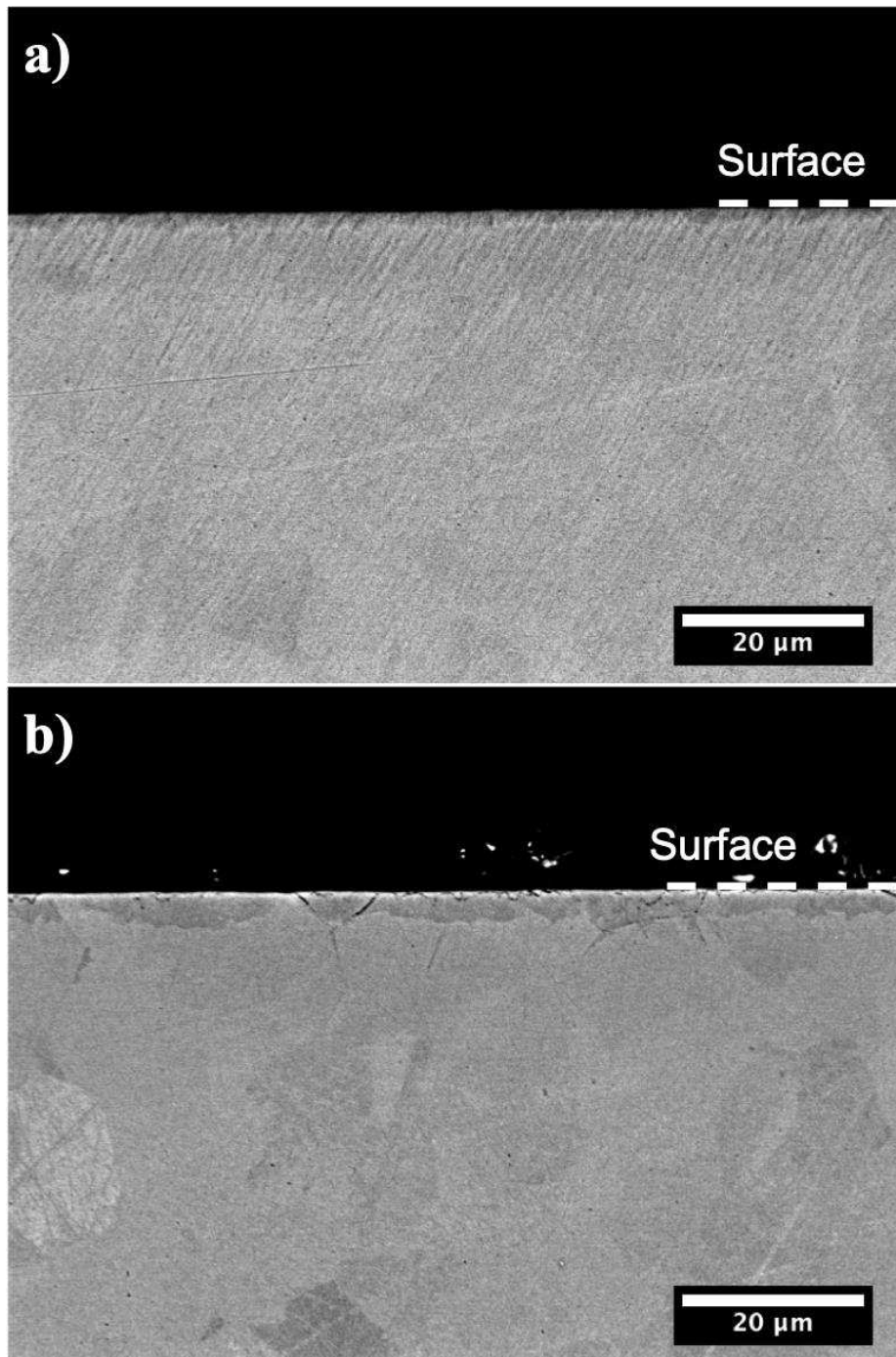683 confidence interval; Surface nitrogen contents of nitrided RA 330® were shown in

684 Ref. **18**

685

686

687

688

Appendix I

Fig. 1 Cross-sectional BSE images of Invar 36® after plasma nitriding at a) 400°C and b) 450°C for 20hrs, at a low magnification to cover the entire hardened zones. No clear features were found corresponding to γ_N-Invar. The "grain structure" observed is most likely owing to different BS electron scattering behavior to different grain orientation.